ELSEVIER

Journal of Applied Geophysics 40 (1998) 139–163

JOURNAL OF APPLIED GEOPHYSICS

Finite-difference time-domain simulation of GPR data

How-Wei Chen *, Tai-Min Huang

Institute of Seismology, Institute of Applied Geophysics, National Chung Cheng University, Ming-Hsiung, Chia-Yi, 621, Taiwan

Received 4 February 1997; accepted 15 April 1998

Abstract

Simulation of digital ground penetrating radar (GPR) wave propagation in two-dimensional (2-D) media is developed, tested, implemented, and applied using a time-domain staggered-grid finite-difference (FD) numerical method. Three types of numerical algorithms for constructing synthetic common-shot, constant-offset radar profiles based on an actual transmitter-to-receiver configuration and based on the exploding reflector concept are demonstrated to mimic different types of radar survey geometries. Frequency-dependent attenuation is also incorporated to account for amplitude decay and time shift in the recorded responses. The algorithms are based on an explicit FD solution to Maxwell's curl equations. In addition, the first-order TE mode responses of wave propagation phenomena are considered due to the operating frequency of current GPR instruments. The staggered-grid technique is used to sample the fields and approximate the spatial derivatives with fourth-order FDs. The temporal derivatives are approximated by an explicit second-order difference time-marching scheme. By combining paraxial approximation of the one-way wave equation (A_2) and the damping mechanisms (sponge filter), we propose a new composite absorbing boundary conditions (ABC) algorithm that effectively absorb both incoming and outgoing waves. To overcome the angle- and frequency-dependent characteristic of the absorbing behaviors, each ABC has two types of absorption mechanism. The first ABC uses a modified Clayton and Enquist's A_2 condition. Moreover, a fixed and a floating A_2 ABC that operates at one grid point is proposed. The second ABC uses a damping mechanism. By superimposing artificial damping and by alternating the physical attenuation properties and impedance contrast of the media within the absorbing region, those waves impinging on the boundary can be effectively attenuated and can prevent waves from reflecting back into the grid. The frequency-dependent characteristic of the damping mechanism can be used to adjust the width of the absorbing zone around the computational domain. By applying any combination of absorbing mechanism, non-physical reflections from the computation domain boundary can be effectively minimized. The algorithm enables us to use very thin absorbing boundaries. The model can be parameterized through velocity, relative electrical permittivity (dielectric constants), electrical conductivity, magnetic permeability, loss tangent, Q values, and attenuation. According to this scheme, widely varying electrical properties of near-surface earth materials can be modeled. The capability of simulating common-source, constant-offset and zero-offset gathers is also demonstrated through various synthetic examples. The synthetic cases for typical GPR applications include buried objects such as pipes of different materials, AVO analysis for ground water exploration, archaeological site investigation, and stratigraphy studies. The algorithms are also applied to iterative modeling of GPR data acquired over a gymnasium construction site on the NCCU campus. © 1998 Elsevier Science B.V. All rights reserved.

Keywords: Ground Penetrating Radar, GPR; simulation; finite-difference; radargrams; staggered-grid

* Corresponding author. Fax: +886-2-05-272-0807; e-mail: seiswei@eq.ccu.edu.tw

0926-9851/98/$19.00 © 1998 Elsevier Science B.V. All rights reserved.
PII: S0926-9851(98)00019-6

1. Introduction

Ground Penetrating Radar (GPR) is a geophysical technique in which an electromagnetic pulse is transmitted into the earth and reflections are received using one or more antennas on the surface. The radar pulse is transmitted, reflected and diffracted by the geological structures and by any anomalous features that may be present in the earth. The reflected and diffracted EM waves are received by a receiver antenna on the earth's surface. The resolution of GPR profiles can be enhanced by stacking over many traces or using post-processing software to effectively suppress unwanted noise. In recent years, GPR data were collected in analog form because of the difficulty in reliably digitizing the data at extremely small (picosecond) intervals. Such a difficulty severely limited the processing and application of GPR data. Until recently, with the advance of digital data acquisition systems (Wright et al., 1989; Davis and Annan, 1989), GPR technology has become possible to resolve practical problems. The kinematic similarities among electromagnetic (radar), seismic waves and sonar have been previously documented by Brekhovskikh (1960), Szaraniec (1976, 1979), Ursin (1983) and others. Thus, under certain assumptions, many approaches for modeling seismic waves may also be applied to radar wave simulation. To more thoroughly understand radar wave propagation phenomena in complex two- and three-dimensional near-surface subsurface structures, numerical modeling becomes an essential tool.

Numerical modeling for electromagnetic methods has been extensively investigated. Various numerical methods include boundary integral equations (Annan, 1973; Raiche, 1974); frequency domain volume integral equations (Hohmann, 1975; Weidelt, 1975; Wannamaker et al., 1984); finite-elements (Coggon, 1971; Silvester and Haslam, 1972; Kuo and Cho, 1980; Pridmore et al., 1981) and finite-differences (Goldman and Stoyer, 1983; Oristaglio and Hohmann, 1984; Adhidjaja et al., 1985). Among all the available methods, relatively few papers have been published concerning the modeling of GPR responses for computing synthetic radargrams. Until recently, Goldman (1994) and Cai and McMechan (1995) demonstrated ray-based modeling algorithms of bistatic (constant-offset) GPR profiles. Zeng et al. (1995) presented a similar scheme for the simulation of monostatic (zero-offset) radar time section. Comparison of the ray- and wave-equation based Fourier method for the simulation of field data was also presented by Zeng et al. (1995). The primary limitation of ray-based modeling is that diffractions from sharp corners or truncation features (such as faults) are not included. Fourier methods (Stolt, 1978; Claerbout, 1985) provide a wave equation approach for modeling the diffraction response. However, the major limitations are that the propagation velocity is assumed to be constant and there is no attenuation. Only a flat free surface, and only the band-limited impulse responses of the model are produced. The direct air and ground waves are not modeled by algorithms published by Cai and McMechan (1995) or by Zeng et al. (1995).

This paper presents a wave-equation based finite-difference solution to the damped scalar wave equation for computing synthetic radargrams to compensate for the limitations of ray- and Fourier algorithms. Finite-difference modeling is chosen because it is a direct numerical approximation of the wave equation. Finite-difference simulation functions well with laterally heterogeneous media, it is equally feasible for both seismic modeling and inverse propagation computations and the computational time for a given grid size is independent of model complexity. Also, full wave fields are propagated without the necessity of prior specification of each wave type to be included. Numerical properties such as grid dispersion (Alford et al., 1974), edge effects (Clayton and Engquist, 1977) and stability problems (Mitchell, 1969), which are associated with different numerical methods, must be first considered. The disadvantage of this method is that it requires a large amount of

computer memory. However, satisfactory output can be obtained with finite-differences if sufficient care is given to those requirements that may appear during computing.

Oristaglio and Hohmann (1984) used an explicit finite-difference solution to simulate transient (time-domain) electromagnetic (TE) responses. Since they neglect displacement current, the fields are diffusive in behavior. However, for GPR frequencies (>5–1200 MHz), the displacement (polarization) properties dominate the conductive properties for many geological materials (Davis and Annan, 1989) with low conductivity. Under such a circumstance, wave propagation dominates diffusion (Stratton, 1941). Lab measurements also support such conclusion (Topp et al., 1980). Therefore, Maxwell's equations can be reduced to the damped scalar wave equation and to simulate the propagating effects of radar waves (cf. eq. 1, Oristaglio and Hohmann, 1984).

Direct time-domain modeling in the approach presented herein differs from those of Lively-brooks and Fullager (1994), Roberts and Daniels (1994), and Wang and Tripp (1996) who worked directly with the coupled first-order equations by the second-order, finite-difference scheme. Their work follows the finite-difference approach of Yee (1966). Our work is based on a second-order equation of the de-coupled electric field or magnetic field, derived from Maxwell's equations. Pridmore et al. (1981) proposed a similar formulation based on finite-element approximation. The following sections present a detailed derivation of the damped scalar wave formulations.

This work demonstrates the capability of simulating GPR data that primarily contains electric field responses. The secondary effects, such as induced magnetic fields, are not explicitly considered. A further objective is to investigate the effects of attenuation on synthetic radargrams. As generally known, the attenuation remains essentially constant at different conductivities, but increases rapidly at frequencies exceeding 100 MHz because of water content. To alleviate the computational boundary effects, composite absorbing boundary conditions are carefully designed and rigorously checked for the numerical behavior of 2-D wave propagation problems. Both simple and complicated numerical models for various applications demonstrate the necessity of incorporating attenuation effects into the numerical simulation of radar recorded in the field. Field data comparisons are also presented to verify the feasibility of our GPR data numeric simulators.

Our work is divided into two parts, each involving a series of computations. The first part focuses on the numerical aspects of a staggered-grid finite-difference computation and on implementing composite absorbing boundary conditions. The numerical characteristics of various non-reflecting boundary conditions are systematically analyzed and compared. Several interesting observations concerning the consequences of selecting different absorbing mechanisms are also discussed. The second part of our work demonstrates the feasibility of the radar modeling scheme through synthetic examples and field data applications. Finally, synthetic common-shot, constant-offset, and zero-offset radar profiles are demonstrated to mimic different types of radar survey modes including reflection profiling, wide-angle reflection and refraction (WARR), and transillumination modes.

2. Methodology

The following sections present the mathematical foundation for numerical solution of partial differential equations. Developing a numerical implementation of the time-domain solution with staggered-grid finite-difference approximation is also proposed for simulating electromagnetic wave propagation in 2-D media.

2.1. Theory

Electromagnetic (EM) wave field propagation phenomena within linear, isotropic near-

surface geological materials are governed by Maxwell's curl equations and the constitutive equations (Nabighian, 1991):

$$\nabla\times\boldsymbol{H}(\boldsymbol{r},t)=\boldsymbol{J}(\boldsymbol{r},t)+\frac{\partial\boldsymbol{D}(\boldsymbol{r},t)}{\partial t}$$
$$=\boldsymbol{J}_{\mathrm{s}}(\boldsymbol{r},t)+\varepsilon(\boldsymbol{r})\frac{\partial\boldsymbol{E}(\boldsymbol{r},t)}{\partial t}+\sigma(\boldsymbol{r})\boldsymbol{E}(\boldsymbol{r},t), \tag{1a}$$

$$\nabla\times\boldsymbol{E}(\boldsymbol{r},t)=-\frac{\partial\boldsymbol{B}(\boldsymbol{r},t)}{\partial t}=\mu(\boldsymbol{r})\frac{\partial\boldsymbol{H}(\boldsymbol{r},t)}{\partial t}. \tag{1b}$$

where $\boldsymbol{H}$ denotes magnetic field intensity (A/m), $\boldsymbol{J}$ represents total electric current density (A/m^2), $\boldsymbol{E}$ is electric field intensity (V/m), $\boldsymbol{B}$ denotes the magnetic induction (T or Wb/m^2; $\boldsymbol{B}=\mu\boldsymbol{H}$), and $\boldsymbol{D}$ represents the electric dipole moment (C/m^2; $\boldsymbol{D}=\varepsilon\boldsymbol{E}$). $\boldsymbol{J}$ is the sum of the conduction current density ($\boldsymbol{J}=\sigma\boldsymbol{E}$) and source electric current density ($\boldsymbol{J}_{\mathrm{s}}$). The vector quantities in the above equations are time and space dependent. In addition, σ, ε, and μ denote the complex electric conductivity (mS/m), the electric permittivity (F/m) and magnetic permeability (H/m) of the medium, respectively. We assume that σ, ε, and μ are all time, temperature, and pressure invariant, but may vary spatially.

The EM wave field can be taken as the superposition of orthogonal polarized components: transverse electric (TE) and transverse magnetic (TM) modes. Taking the vector product, $\nabla\times\nabla\times\boldsymbol{E}$, the curl of the vector $\boldsymbol{E}$ field in Eq. (1b), and substituting Eq. (1a) into Eq. (1b), a vector wave equation can be obtained for the secondary transverse electric fields, i.e.:

$$\nabla(\nabla\cdot\boldsymbol{E}(\boldsymbol{r},t))-\nabla^2\boldsymbol{E}(\boldsymbol{r},t)$$
$$=-\mu(\boldsymbol{r})\left[\varepsilon(\boldsymbol{r})\frac{\partial\boldsymbol{E}(\boldsymbol{r},t)}{\partial t^2}+\sigma(\boldsymbol{r})\frac{\partial\boldsymbol{E}(\boldsymbol{r},t)}{\partial t}+\frac{\partial\boldsymbol{J}_{\mathrm{s}}(\boldsymbol{r},t)}{\partial t}\right], \tag{2}$$

assuming that there is a constant amount of free charge and that the conductivity in the medium is not a function of the rate of change of the electric field in space. Recognizing the fact that $\nabla\cdot\boldsymbol{E}=0$ for homogeneous regions, Eq. (2) becomes a decoupled wave equation for the electric field in the time domain. In 2-D modeling, the dipole antennas are normally oriented so that the electric field is polarized parallel to the target strike direction. For a negligible magnetic loss, the imaginary component of the complex relative dielectric permittivity is zero and the magnetic permeability is assumed to be that of free space ($\mu=\mu_0$). In most cases, the relative susceptibility, μ/μ_0, can be taken to remain constant except where metallic objects or minerals are present in abundance (Telford et al., 1976).

For a 2-D medium, a line source on the surface of the earth and the electric field response is described by a decoupled TE field. The equation then becomes:

$$\frac{\partial^2\boldsymbol{E}}{\partial^2 x}+\frac{\partial^2\boldsymbol{E}}{\partial^2 z}=\mu\varepsilon\frac{\partial^2\boldsymbol{E}}{\partial t^2}+\mu\sigma\frac{\partial\boldsymbol{E}}{\partial t}+\mu\frac{\partial\boldsymbol{J}_{\mathrm{s}}}{\partial t}. \tag{3}$$

The first term on the right-hand side of the wave Eq. (3) represents the displacement of charge caused by the field. The second term, the damping term, describes the conduction of charge caused by the applied electrical field. The third term can be treated as a source excitation term that is the applied electric field. For a lossy dielectric medium at high frequency, the attenuation factor α, that is, the decibel loss per meter, and the phase constant β are frequency dependent and can be related to the quality factor (Q) by (e.g., von Hippel, 1954):

$$\alpha=\frac{\omega}{c_{\mathrm{o}}}\left[\frac{k_e k_m}{2}\left(\sqrt{1+\tan^2\delta}-1\right)\right]^{1/2} \tag{4a}$$

$$\beta=\frac{\omega}{c_{\mathrm{o}}}\left[\frac{k_{\mathrm{e}} k_{\mathrm{m}}}{2}\left(\sqrt{1+\tan^2\delta}+1\right)\right]^{1/2} \tag{4b}$$

where $Q=(\tan\ \delta)^{-1}=(\sigma/\omega\varepsilon)^{-1}$, k_e and k_m denote the real parts of the relative permittivity $(=\varepsilon/\varepsilon_o)$ and relative permeability $(=\mu/\mu_o)$ of the material. In a vacuum, the wavelength denotes λ_o and the wave travels with the velocity of light, $c_o=0.3$ m/ns with the angular frequency ω. The propagation of the $\boldsymbol{E}$ field with displacement is dispersive with phase velocity $\nu=\omega/\beta$. The term α^{-1} is generally expressed as the attenuation distance (or skin depth) over which the wave field strength decays to $e^{-1}(=0.368)$ of its initial amplitude value.

For material with low conductivity and at sufficiently high frequency, displacement current dominates over the conduction current and EM waves propagate. The radar signal propagating in low-loss ($\tan\ \delta \ll 1$) common soil and rock materials are related to the real part of the ε. The frequency dependence of the dielectric constant and conductivity are small, and for practical purposes, these parameters can be treated as constants. The wave velocity $c=(\mu\varepsilon)^{-1/2}$, and the coefficient of the damping term in Eqs. (4a) and (4b) can be rewritten as $\mu\sigma=(2\pi f\tan\delta)/c^2$, where f denotes the frequency. The loss tangent $\tan\ \delta$ is defined as the ratio of the imaginary and real part of the complex dielectric permittivity or alternatively the ratio of conduction current density to displacement current density. Our current approach only considers the first-order effects of TE wave field responses in the ground. The wave Eq. (3) becomes the electric field (E_e) lossy wave equation:

$$\frac{\partial^2 E_e}{\partial^2 x}+\frac{\partial^2 E_e}{\partial^2 z}=\frac{1}{c^2}\frac{\partial^2 E_e}{\partial t^2}+\frac{2\pi f\tan\delta}{c^2}\frac{\partial E_e}{\partial t}+\frac{1}{\varepsilon c^2}\frac{\partial J_s}{\partial t}. \quad (5)$$

Because GPR systems normally operate in the frequency range between 25 to 1200 MHz, the ground may behave as a dielectric medium in which the velocity remains constant and the conductivity is less than 100 mS/m (Davis and Annan, 1989; Bogorodsky et al., 1985). Under such conditions, the associated attenuation may be considered separately from the propagation velocity and radar waves behave like seismic acoustic waves. Notice that Eq. (5) is the damped wave equation similar to the equation proposed by Sochachi et al. (1987) to eliminate any unwanted reflections from artificial numerical boundaries.

Numerical solutions of TE wave field responses from 2-D structures are achieved by approximating the differential equation through the finite-difference method. We also assume that the numerical model used should be invariant along strike (i.e., perpendicular to the survey line).

3. Numerical implementation

Eq. (5) is used to derive a finite-difference equation based on numerical operators to approximate the partial derivatives. The model is discretized into a uniform grid with a grid spacing of Δh. Each grid point is assigned a veloc-

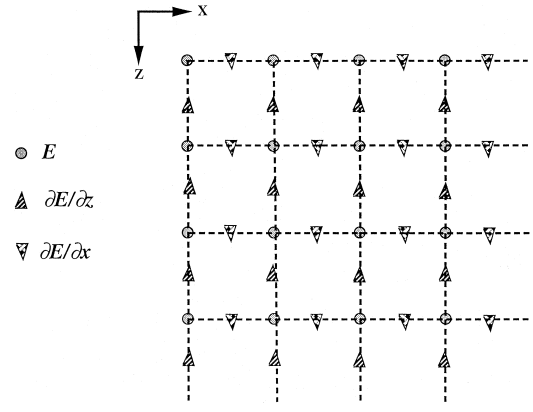

Fig. 1. A spatially staggered-grid system to model transverse electric waves in two-dimensional Cartesian coordinates. The **E** field is defined at each sampling location whereas electric gradients are evaluated half way between sampled positions.

ity (e.g., relative dielectric permittivity ε) and an attenuation coefficient (or equivalently, the loss tangent, Q, or electric conductivity). The spatial derivatives are approximated by a fourth-order difference scheme. The temporal derivatives are approximated by second-order central differences. A spatially staggered-grid technique is also adopted to specify material properties and to sample the $\boldsymbol{E}$ fields and their derivatives on the grid (Fig. 1). Dablain (1986) and Levander (1988) demonstrated that staggered-grid high-order schemes are better than low-order schemes for modeling seismic waves. Such a numerical scheme simulates dispersion properties better than the conventional difference scheme such as a second-order scheme in space and time (Robertsson et al., 1994).

Explicit fourth-order finite-difference formulation of a damped scalar wave Eq. (5) can be written as:

$$\begin{aligned} E_e(i,j,,t+1) = \frac{1}{1+A}\Bigg\{ C_o\Bigg[\frac{-1}{12}\big(E_e(1+2,j,t) \\ + E_e(i-2,j,t) + E_e(i,j+2,t) \\ + E_e(i,j-2,t)\big)\Bigg] + \frac{4}{3}\Bigg[\big(E_e(i+1,j,t) \\ + E_e(i-1,j,t) + E_e(i,j+1,t) \\ + E_e(i,j-1,t)\big) \Bigg] + \Bigg[2E_e(i,j,t) \\ - E_e(i,j,t-1) + \big(A - \frac{20}{3}\big)E_e(i,j,t)\Bigg]\Bigg\}, \end{aligned} \tag{6}$$

where Δh denotes the grid spacing, Δt represents the time increment, $A = 2\pi\Delta t\, f \tan\delta$, and $C_o = (c^2\Delta t^2)/(\Delta h^2)$. Indices t, i, and j correspond to time and space coordinates along x- and z- directions, respectively. The leap-frog scheme (Kreiss and Oliger, 1972) for Eq. (5) is used to solve for the updated wave field from wave fields at previous two time steps.

Alford et al. (1974) also indicated that the stability criteria for fourth-order accurate spatial derivatives and second-order accurate temporal derivatives scheme is:

$$\Delta t \le \sqrt{\frac{3}{8}}\,\frac{\Delta h}{V_{\max}}, \tag{7}$$

where $V_{\max}$ represents the maximum velocity of the waves in the media. The maximum time increments for time-marching the finite-difference equation must not exceed Δt. Any value of Δt that satisfies the lossless stability condition will also be stable for the lossy case. Our numerical experiments also confirm such a conclusion. To avoid numerical grid anisotropy for a given spatial sampling, the grid increment should be:

$$\Delta h \le \frac{V_{\min}}{5 f_{\max}}. \tag{8}$$

For a particular model, the grid spacing should be chosen such that approximately five or more grid points per wavelength are necessary at the dominant frequency (typically 1.5 times the effective center frequency). From our experience, the grid spacing should not exceed $1/10$ of the shortest wavelength anticipated for a particular model in order to achieve good accuracy and avoid grid dispersion.

Initial conditions at the first two time steps are defined through the electric field pattern at $t = 0$ and $t = \Delta t$. Assume that the source excitation current waveform is a Ricker pulse wavelet

$$J_s(t) = \sqrt{\frac{e}{2\theta}}\, e^{-\theta t^2}, \tag{9}$$

where θ denotes a constant that determines the peak-to-peak time interval of $J_s(t)$. It is sufficient to choose the dominant frequency at $f = \sqrt{2\theta}$. The factor $\sqrt{e/(2\theta)}$ is used to normalize the peak amplitude of $J_s(t)$ to 1.

Composite non-reflecting or absorbing boundary conditions (ABC's) are developed for numerical calculation of radar wave propagation. The numerical absorbing boundaries were primarily designed to simulate transmission of energy at the edges of the computational do-

main such that no artificial waves would be reflected. By combining the paraxial approximation of a one-way wave equation (A_2) and a damping mechanism (sponge filter), we obtain methods that effectively absorb various types of waves (Fig. 2). Each type of ABC has two separate modified methods. In the following sections, we first demonstrate the behavior of each absorbing mechanism and its corresponding artifacts. The non-physical waves can be sufficiently suppressed when composite boundary conditions are applied.

The Clayton and Engquist (1977) A_2 condition is restricted to waves impinging on the artificial boundary at angles up to 30°. As generally known, the amount of the energy reflected from the boundary increases as the angle of incidence increases. To compensate for such an angle-dependent A_2 condition, a modified floating A_2 condition is proposed and tested. A dipping-layer model (Fig. 3) is created to test the behavior of the fixed and floating A_2 absorbing boundary conditions. The source is intentionally placed on the surface and close to the edge of the model. Under such situation, the incidence angle of the waves travelling to the computational domain boundary is relatively large while the angles of incidence for reflected and transmitted waves travelling to the opposite side of the model boundary are relatively small.

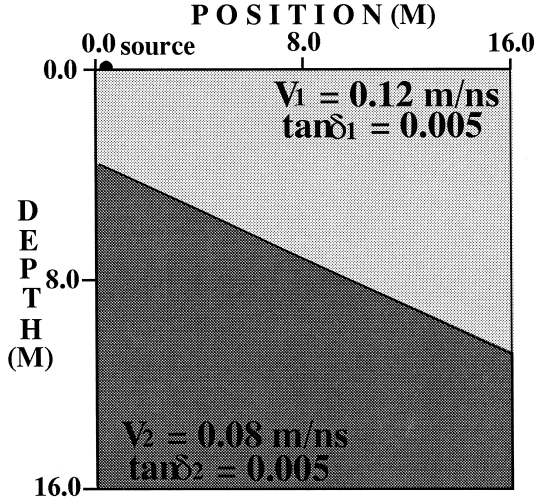

Fig. 3. A dipping-layer model used to test non-reflecting A_2 boundary conditions. The source (large dot) is located at the surface but close to the edge of the numerical boundary. The receiver array is located along the free surface. Reflections are produced from the boundary separating two different types of rocks with different propagating velocity, although they have the same Q values.

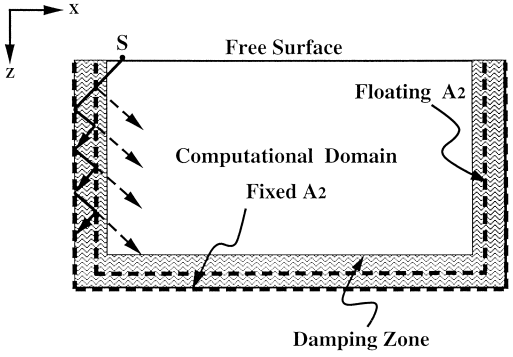

Fig. 2. Configuration of composite absorbing boundaries proposed for this study. Dashed lines denote the fixed and floating A_2 absorbing boundaries. The shaded region around the computational domain is the area where damping mechanisms are applied. Figs. 4 and 5 depict the radar waves emit from source S and generate various artificial waves within the boundaries. Artifacts associated with such boundary conditions are indicated by ray paths. These artifacts are sufficiently suppressed when composite boundary conditions are applied.

The simulation of wave propagation phenomena can be computed and visualized via a series of fixed-time snapshots through the model domain or directly by the theoretical calculation of radar responses recorded at each pre-defined station location (radargrams) in the space–time domain. The behavior of each type of absorbing boundary condition can be evaluated by examining the calculated responses both from wave field snapshots (Fig. 4) and the corresponding GPR radargrams (Fig. 5). Fig. 4 illustrates the computational artifacts without absorption (Fig. 4a) and their suppression associated with boundary conditions by comparing results obtained from floating A_2 (Fig. 4b), fixed A_2 (Fig. 4c), and a combination of both absorbing algorithms (Fig. 4d). The artifacts are related to

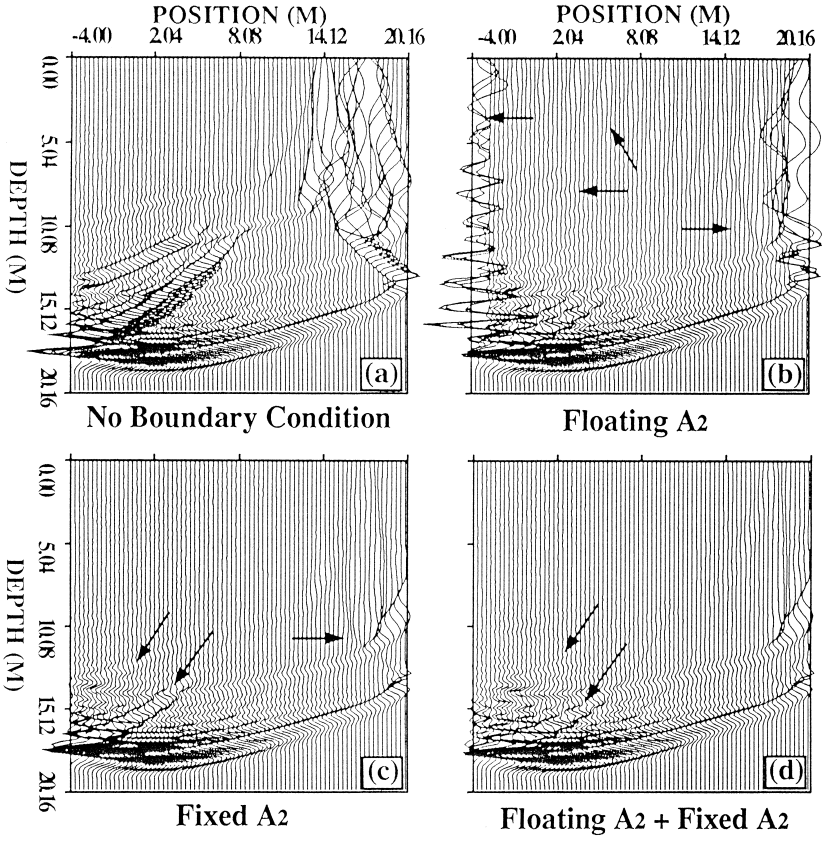

Fig. 4. Fixed-time (225 ns) wave field snapshots are computed for the model of Fig. 3. For comparison, radar wave responses without absorbing boundary are shown in (a). Variations in radar responses due to different nonreflecting boundary conditions (b to d) are discernible. Arrows denote the artifacts related to their corresponding absorbing algorithms. The non-physical waves generated from fixed and floating A_2 are effectively reduced after applying both conditions. The waves reflected, transmitted, and multiple reflections between fixed and floating A_2 boundaries can be further suppressed using a damping mechanism within the specified damping zone. All panels have the same amplitude scaling factor. Fig. 5 presents the corresponding radargrams.

the algorithm since they disappear when the algorithm is changed. Fig. 5 contains the corresponding synthetic radargrams for the same wave field, recorded on the surface. A noticeable ringing effect is more pronounced (Figs. 4b and 5b) for floating A_2 due to leakage of trapped waves. However, such phenomena were effectively suppressed when a fixed A_2 condition was superimposed at the edges of the model. Although combining two algorithms works well (Fig. 4d), some small nonphysical reflections from the ABC's still persist.

Cerjan et al. (1985) presented a spatial sponge filter that employs a damping mechanism (Kosloff and Kosloff, 1986; Sochachi et al., 1987) to systematically eliminate the wave amplitude in a strip along the boundary of the numerical mesh. Israeli and Orszag (1981) also used a 'Newtonian cooling' or perturbation term scaled by a damping coefficient for the wave equation to improve absorption of outgoing waves. The absorbing buffer region has an artificial taper with an exponential function of $\exp(-k_b(N-n_i)^2)$ to reduce waves reflected back into the computational domain. Numerical experiments indicate that artificial damping can be used to effectively suppress the unwanted nonphysical waves. The frequency-dependent

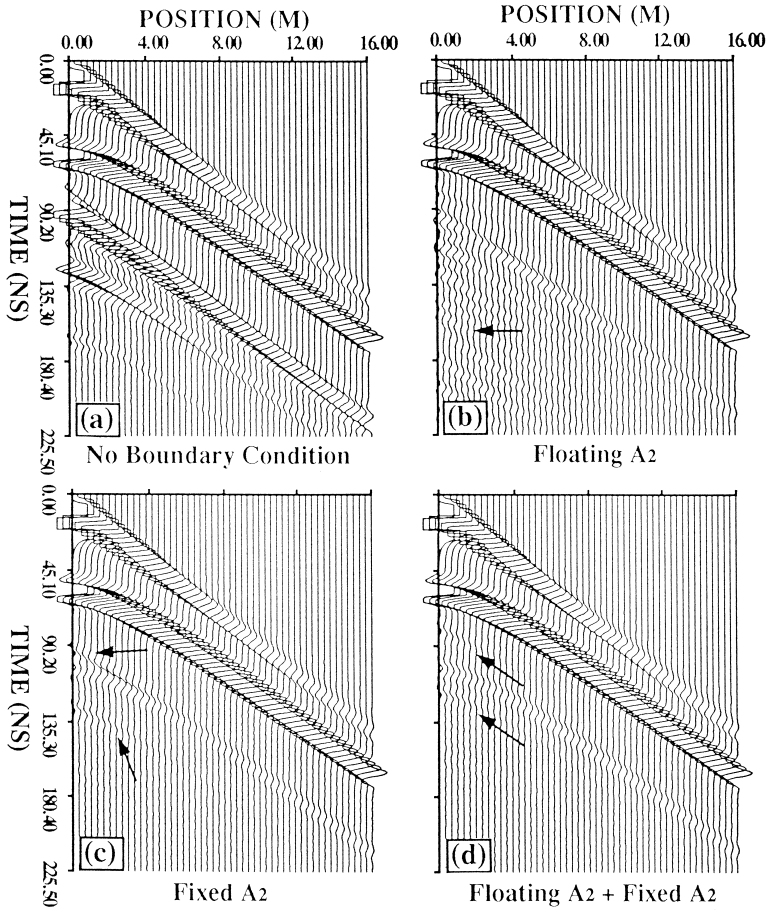

Fig. 5. Synthetic time sections calculated from the model (Fig. 3) for various types of A_2 absorbing boundary conditions. Radargrams are recorded along the earth's surface. Arrows in b to d are non-physical arrivals due to the imperfection of the boundary conditions. Those non-physical reflections from the boundary of the computational domain are considerably reduced by superimposing two different A_2 algorithms in (d). However, small edge reflections from boundaries are still visible. Fig. 4 depicts the corresponding snapshots.

absorption can be further enhanced by increasing the attenuation properties exponentially within the damping region toward the edges. The loss tangent within the damping zone is altered according to $\tan \delta' = \tan \delta \cdot \exp(-k_1(N - n_i)^2)$ where both k_b and k_1 are constant and N is the width of the absorbing region. We also tuned the impedance contrast in the absorbing region to minimize reflections. Synthetic radargrams in Fig. 6 illustrate the two possible combinations of absorbing methods. Fig. 6a summaries the results after applying both artificial damping and physical attenuation properties within the absorbing region. Fig. 6b demonstrates how to combine the A_2 and sponge filter approach. Both cases produce nearly the same result, indicating that the composite boundary condition may effectively suppressed those unwanted waves from the numerical model. The composite absorbing boundary conditions are used in the following synthetic and field data applications. The proposed method seems to work quite well with acoustic propagation problems. However, the algorithm requires some further investigation if coupled electromagnetic wave fields are considered.

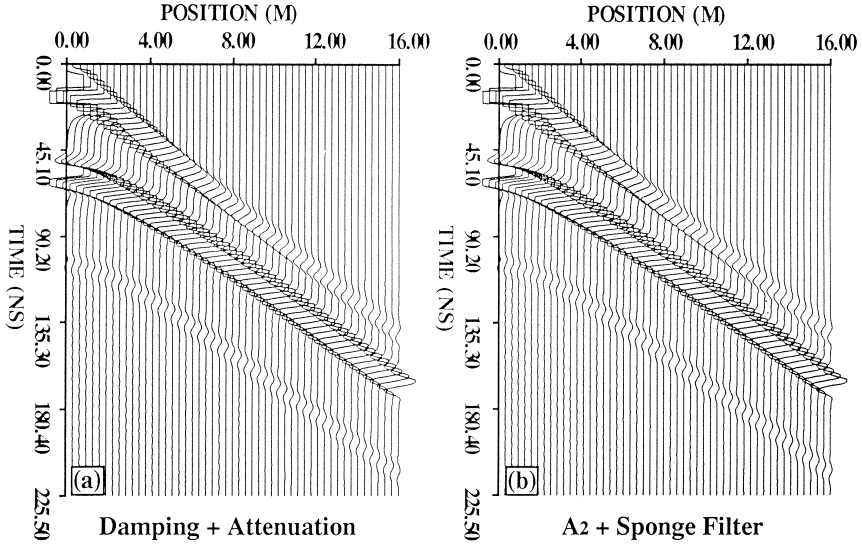

Fig. 6. Synthetic radar responses calculated from a different combination of absorbing mechanisms. (a) Synthetic radargrams calculated from the model with the combination of damping and alternating attenuation properties in a region around the periphery of the computational domain. The radargrams in (b) are the result of applying all the available boundary conditions.

The synthetic example in Figs. 3 and 4 and 4–6, reveal that the artifact due to the limitation of the angle-dependent A_2 condition can be somewhat alleviated when combined with the damping condition. One the other hand, the restriction on determining the width of the damping region is frequency-dependent. The higher the dominant frequency of the computed response requires that a narrower width of the damping zone be used. The advantage is that any combination of paraxial approximation of A_2 and damping algorithms actually reduces the width of the absorbing region. For example, in the synthetic test model of Fig. 6, we used 20 grid points for the damping method, whereas 10 grid points were used after A_2 conditions were included.

4. Forward modeling of radar data

The 2-D modeling algorithm described above enables a synthesis of the radar response for an extensive variety of realistic cases in GPR exploration. In the following synthetic and field data applications, all models are defined through electrical properties and attenuation factors. The computed synthetic radargrams do not show absorbing areas surrounding the numerical model. Although the Q model can be specified independently in contrast to the velocity model, for simplicity, a Q boundary defined in this work is assumed to be the same as the velocity boundary. The following sections present the synthetic examples first followed by the field data application.

4.1. Synthetic examples

The second part of this paper focuses on simulating radar responses from a specified model and recording at any particular antenna layout, according to actual field data acquisition geometry. The recorded field data can be arranged according to the geometrical relationship between transmitter and receiver. The recorded time section can be generally classified into common-source, common-offset, and common-

midpoint reflection profiles. Various synthetic examples demonstrate the capability of simulating different transmitter and receiver configurations and their corresponding radar profiles. To simulate primarily reflected radar waves and to accelerate the entire iterative modeling procedure, a hypothetical simulation scheme, base on the exploding-reflector concept, can be conducted. For practical purposes, using the exploding-reflector concept to simulate a zero-offset section is advantageous when performing a computer simulation of field data. The limitations of the exploding-reflector approach are discussed when simulating both field and synthetic radar gathers.

4.2. Variable recording geometries

Fig. 7 depicts three cylindrical objects (pipes) buried at different depths and surrounded by a relatively homogeneous argillaceous sandstone. Three data acquisition modes are illustrated according to their different transmitter and receiver configurations. The ray paths in Fig. 7 illustrate the possible propagation paths which correspond to the main reflections observed in the different gathers. A 400-MHz antenna was used to collect radar reflection data with a 70-ns time window. Fig. 8 presents the results of simulating actual responses based on different field acquisition geometry. Clearly, the reflections generated on the common-shot gather (Fig. 8a), zero-offset (constant-offset at which both antennas coincide) (Fig. 8b), and exploding-reflector model (Fig. 8c) were predicted from finite-difference modeling. The amplitude of the radar reflections is relatively strong due to the high impedance contrast and distinct differences in the electrical properties between metal (tan $\delta = 10^{7}$) and argillaceous sandstone (tan $\delta = 10^{-3}$). The field experiments also confirm such observations. The radar time section in Fig. 8c was constructed on the basis of the exploding-reflector concept under the condition that the media velocity must be multiplied by two. Notably, the direct arrivals are not predicted by such an algorithm. Comparing arrival times, moveout curvature, amplitude of reflected and, typically, the multiply reflected radar wave reveals the fundamental differences among three

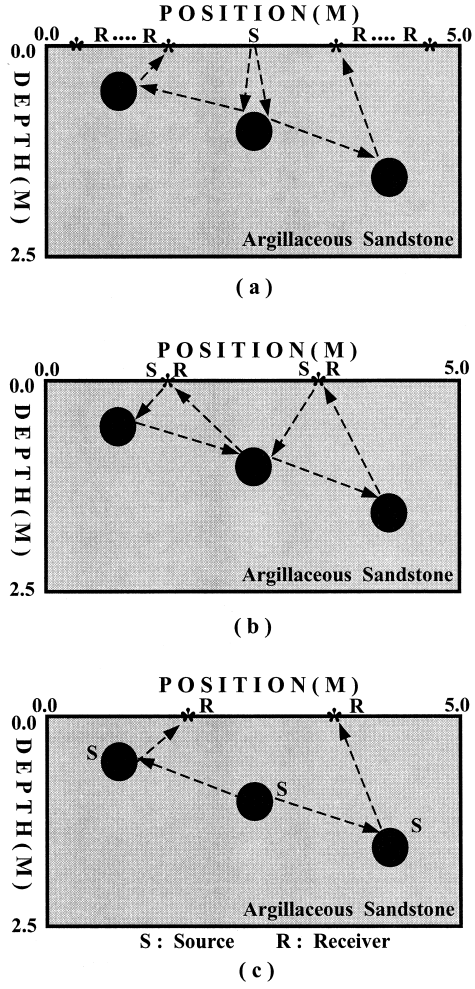

Fig. 7. Model with three cylindrical metal pipes buried at a depth of 0.5, 1.0 and 1.5 m, respectively. These pipes are surrounded by a homogeneous argillaceous sandstone. The model has 501×251 grid points along *x*- and *z*- directions, respectively. Common-source (a), zero-offset (b) or constant-offset radar gathers can be constructed by the radar simulator. The primary reflection can be simulated via the exploding-reflector concept (c). S and R represent transmitter and receiver locations being used to produce synthetic radargrams. Dashed lines represent the possible ray paths which corresponding to primary and multiple reflections presented in Fig. 8.

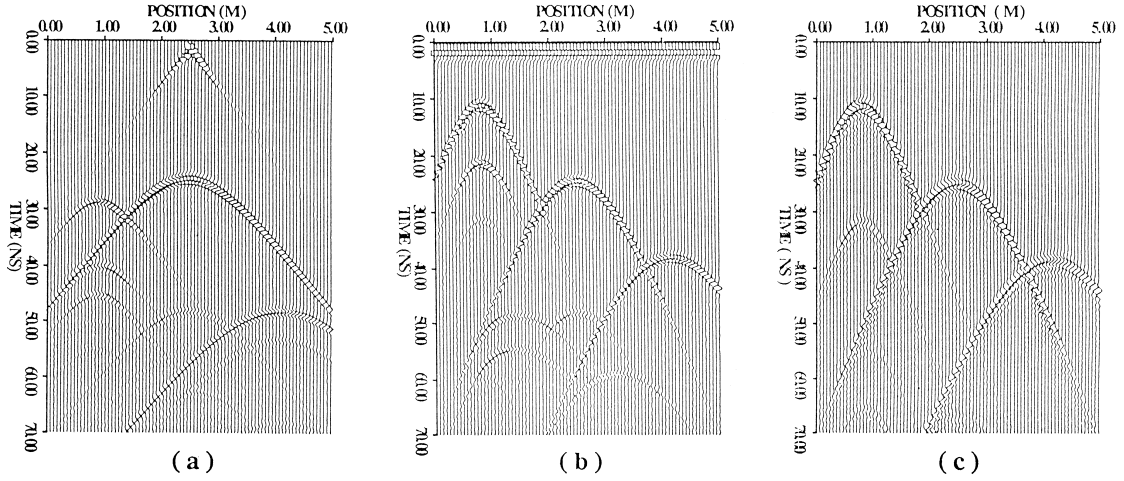

Fig. 8. Synthetic radar profiles obtained from the model (Fig. 7). Different source and receiver configurations produce different radar responses. Multiple reflections obtained from different antenna geometry are different for total travel time, amplitude, and waveforms.

simulated time sections. Such differences are primarily produced from different algorithms due to different propagation path effects. It is important to choose the right radar wave simulator when a particular radar section is recorded using a specific transmitter and receiver configuration.

Fig. 8 illustrates the limitations of simulating a zero-offset radar section based on the exploding-reflector concept. Comparing Fig. 8b and

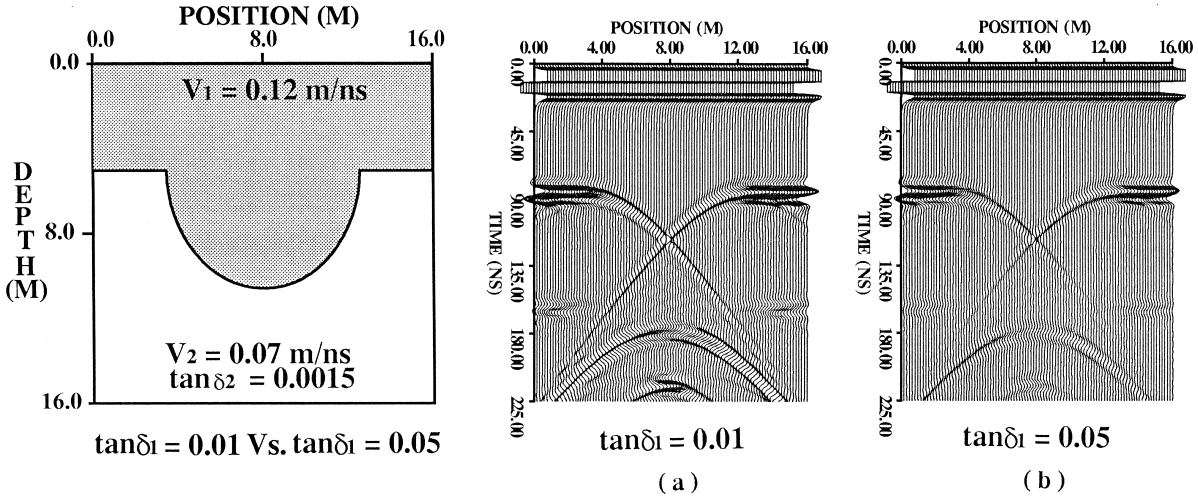

Fig. 9. The model (left), representing an internal void space beneath airport or highway pavement, is adopted to calculate radar responses for engineering applications. Comparison of the calculated radar responses between low (middle) and high (right) loss tangents (tan δ) properties in the subgrade soil are shown. Variations in the radar signal caused by differences in the electrical properties in the soil-refilled void produces a radar signal with different amplitudes, mainly as a result of attenuation.

Fig. 8c obviously reveals that the exploding-reflector model fails to simulate multiple reflections. Such a difference in multiple reflections, e.g., the ray paths of the first multiple generated from the right-most pipe is illustrated in Fig. 7. The total two-way travel time of the multiple reflections generated on the zero-offset section differs from those on the exploding-reflector model. The ray paths are different as Fig. 7 indicates. The waveform and its amplitude of the first multiple is obviously different. This is primarily because the exploding-reflector model predicts the wave emitted by both sides of the interface to have the same polarity. In contrast, the physical reflection coefficients from opposite sides should have opposite polarities. Thus, some precaution is required when interpreting field and synthetic data. If lateral velocity variations exist, the reflections produced by objects surrounding the main reflector may not be accurately predicted by the exploding-reflector model. Such phenomena can also be observed in this example.

4.3. Engineering applications

In geotechnical applications, GPR can be used to detect disturbed soils and backfills as well as to locate void and delaminations beneath concrete structures, e.g., bridge decks, highways, and airport pavements. These objects exhibit markedly different electrical properties compared to surrounding materials. For example, a void beneath pavement is formed because of leaks and ex-filtration of the soil, and is later filled with low dielectric materials such as loose sand or silt. The electromagnetic constants may vary because of changing environmental conditions. A radar simulation of subsurface and internal voids is computed to predict GPR responses in the field survey. The synthetic model (Fig. 9) was represented by a low-velocity (high dielectric) layer filled with high-velocity (low dielectric) material. The loss tangent in the U-shaped trench is varied to observed the difference in the computed synthetic radargrams (Fig. 9a,b). Amplitude decay caused by the high attenuation medium can be observed. Also observed is a phase change produced from corner diffractions and reflections (at 180 ns). A focusing effect due to the crossing of reflections, at approximately 200 ns is observed as well. Therefore, the possibility of detecting and estimating the size of an existing void beneath concrete airport runways from noisy data sets

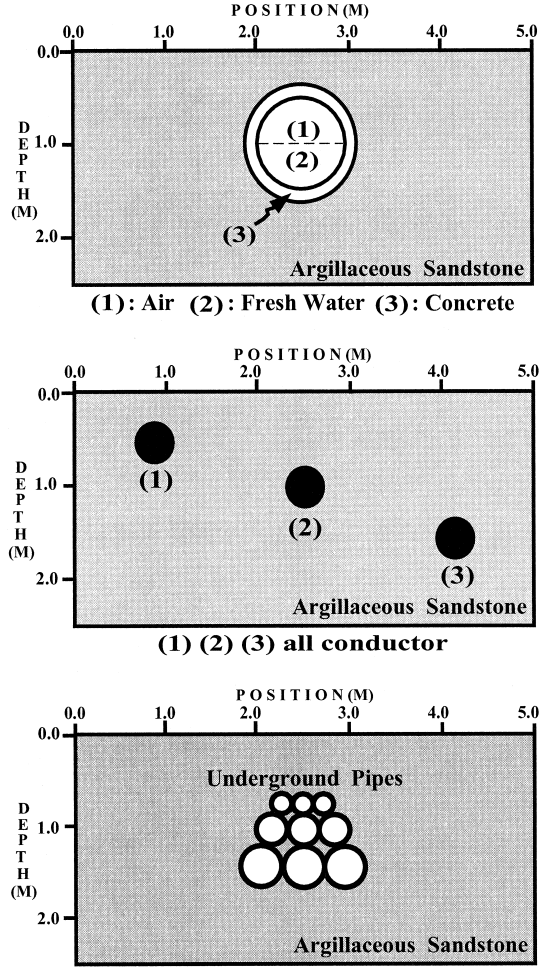

Fig. 10. Numerical models used to investigate their corresponding synthetic radar records (Fig. 11) collected along the surface. Underground fresh water or drainage pipe (upper), reinforcing rebar (middle), and pipes (lower) are used in this study. Both air and water are included in the concrete sewer conduit, which is buried at a depth of 1.0 m. A buried drainpipe or electrical cable pipe system with a variable size ranging from 10 to 20 cm is modeled to investigate the resolution power of radar responses.

can be achieved by using forward modeling procedures. The advantage of simulating the GPR wave field over the ray simulation method can be recognized from the computed responses. Reflections, refractions, diffractions, and multiples are all automatically produced.

4.4. Conduit, metal rod, and pipes

GPR is also frequently used to locate features such as buried pipes, reinforcing rod in concrete structures, and conduits embedded in the ground for water, sewer, electrical cable or gas connections. Locating underground pipes for efficient pipe system management and for avoiding damage during excavation has become a relevant issue in metropolitan areas. Fig. 10 depicts synthetic models that are commonly encountered in such GPR applications. The model includes underground concrete conduits (upper), reinforced metal rods (middle), and pipes (lower). The main targets were assumed to be buried in a homogeneous argillaceous sandstone environment. The loss tangent of the background sand-

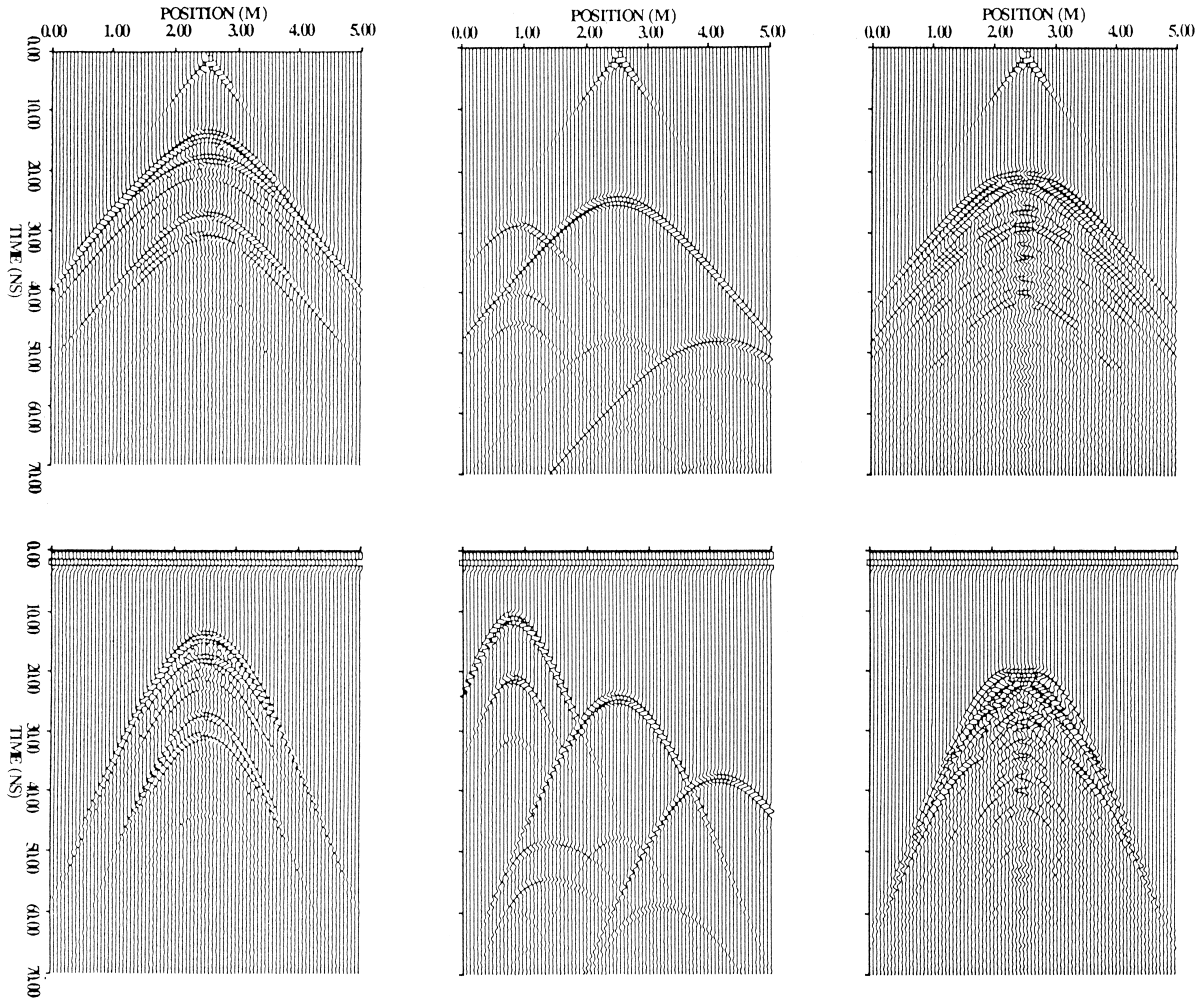

Fig. 11. The radar time sections computed from their corresponding numerical models in Fig. 10. Upper panels, from left to right, are the corresponding common-source gathers. Lower panels are the constant-offset gathers which are frequently used during field data acquisition. A 400 MHz transmitter antenna is located at (2.5,0.0) m and radar data is collected along the earth's surface.

stone is 0.001 with a ground velocity of 0.075 m/ns. The antenna operating frequency used in these cases is 400 MHz. These models are somewhat over simplified to clearly avoid any ambiguous interference from surrounding anomalous objects and to see the main reflections from the major target.

Fig. 11 presents the synthetic radar time sections obtained from the corresponding models (Fig. 10). Common-source (upper panels) and constant-offset (lower panels) radar profiles are generated from finite-difference simulators. For comparison purposes, Fig. 11 presents various radar reflection patterns as a guide for interpreting radar profiles and signatures. The amplitude of reflections from buried conduit and iron rod is rather obvious since the dielectric contrast between these materials and surrounding background material is relatively substantial. The presence of water and air with different dielectric constants produces multiple reflections when electromagnetic waves are propagated into the target. The distinguishable multiples and flat reflections, as found from their radargrams, can be a good indicator for identifying a drainage ditch or sewer system. The radar diffractions from each pipe within the multiple pipe system cannot be resolved even though a relatively high frequency antenna is used. Post-processing techniques can be applied, e.g., migration, to enhance the final image resolution. However, the response from pipes of various sizes produce specific patterns which can be used as indicators when locating an underground pipe system in the field. The lateral amplitude changes and variations in diffraction patterns for various kinds of pipes can be used for further analysis. Therefore, radar simulation can serve as a tool for interpreting different radar responses from different materials and from a variety of shapes and interfaces.

4.5. Archaeological applications

GPR is a practical tool in facilitating the determination of the depth and shape of buried objects and in surveying protected archaeological sites (Bevan, 1991). Forward modeling of synthetic radargrams can be used to interpret radar signatures obtained from the field. The method can accurately estimate the reflected TE wave energy and waveform from the structural characteristics of the burial mound. Many possible models can account for the measured radargrams. However, the number of possible models can be reduced when prior information on the buried structure is available.

The concept that ‘the present is the key to the past’ in physical geology processes can be used to facilitate interpretation of the radar signatures from a typical buried wooden coffin and its related structure of construction. Fig. 12 depicts a schematic feature of a grave type commonly found in Taiwan. The most distinctive feature is the disturbed soil in the filled excavation. The soil filling the grave shaft could have a different electrical and magnetic signature from the naturally undisturbed earth. A wooden or stone coffin could be present at the bottom of the grave shaft. If there is a burial vault of brick or stone, the existence of an air-filled cavity in the brick or stone may offer a relatively large contrast compared to the surrounding soil. If an old coffin is still partially intact, nothing can remain except for bones; there might be air in the void.

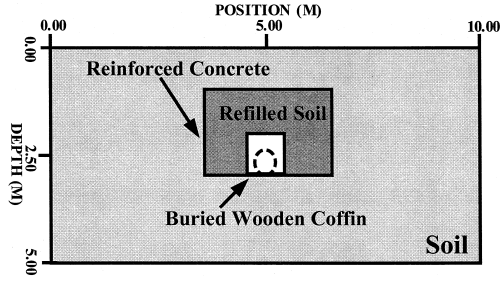

Fig. 12. A generalized model of a buried tomb with features such as a reinforced concrete or a brick chamber and wooden coffin on the floor surface. The tomb has a rectangular shape infilled with disturbed soil. An air-filled cavity inside the coffin produces a fairly strong impedance contrast among the soil, coffin, and void system.

Fig. 13 displays the simulated synthetic radar profiles for an antenna frequency of 200 (left panels) and 100 MHz (right panels), respectively. Common-source (upper panels) and constant-offset (lower panels) radar gathers were generated to compare their radar signatures to major diffractors and reflectors. Both gathers indicate a rather peculiar pattern (at 27 ns) for radar waves reflected from the top of the reinforced concrete vault. Reflections from the top and bottom of the coffin; multiple reflections propagating within the air-filled cavity inside the wooden coffin; diffraction from the corners and interference patterns can be identified from the synthetic radargrams. The relatively 'bright' radar reflections due to a large impedance contrast between the air-filled coffin and soil are good indicators for locating burials. These radar signals may be interfered with the scattered energy from the surrounding soil and can be further attenuated if the grave site does not have a good culvert system to drain underground water. The depth of penetration of a radar wave can be severely limited due to environmental change. The human skeleton generally cannot be directly detected. However, some detectable

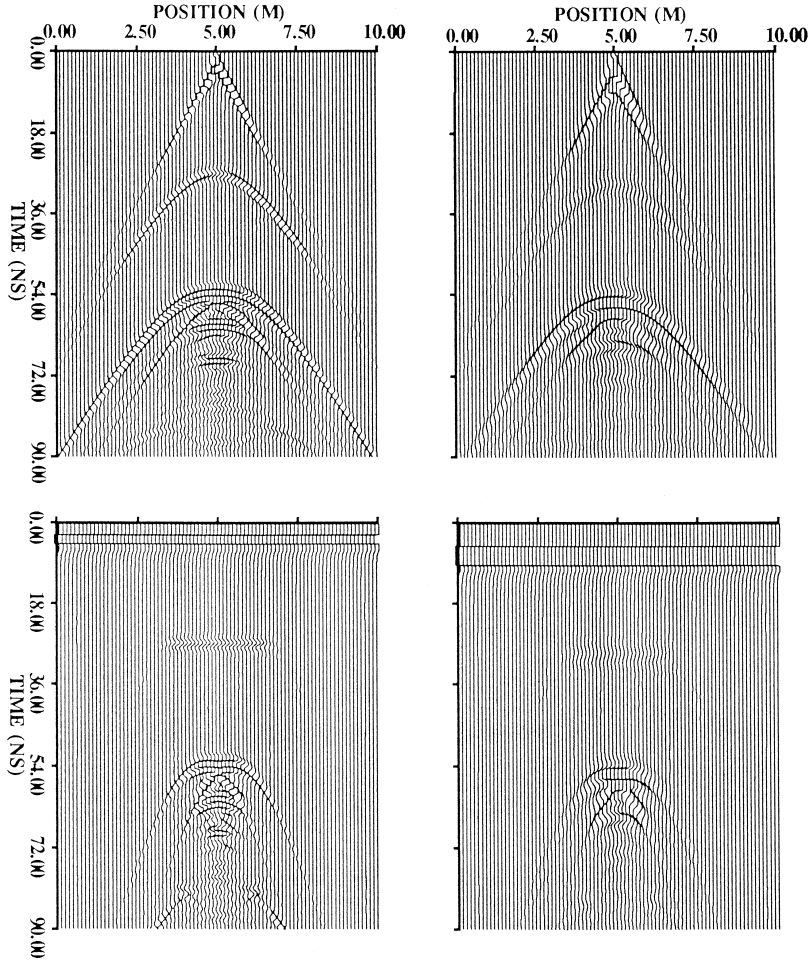

Fig. 13. Synthetic radargrams constructed from the model in Fig. 12. Common-source (upper panels) and constant-offset (lower panels) gathers of electric field responses along the surface with a central frequency of 100 (right) and 200 (left) MHz.

responses from the radar profile might suggest a grave buried under the ground. These features include discontinuous subsurface strata; soil at the bottom of the burial site which is usually much more compact so as to produce a rather strong contrast. The body decay may alter the chemical composition of the surrounding soil. These features can be treated as useful guidance in locating unmarked burials.

4.6. Offset and angle-dependent amplitude and travel time variation

Amplitude variation with offset (AVO), or amplitude variation with incidence angle (AVA) analysis for ground water exploration is another pertinent issue. For AVO/AVA analysis, modeling is used to gain qualitative insight into variation of the amplitude from objective reflections. Radar reflections are produced by changes in electrical impedance in the ground. When GPR is applied, electrical impedance is dominated by changes in the relative permittivity or dielectric constant of the ground. The presence of water content in the pore space of the soil matrix can markedly vary the impedance contrast and attenuation properties of the material. Radar wave simulation results demonstrate that considerable variation of dynamic properties, such as decreased amplitude caused by low Q and temporal shift caused by physical wave dispersion phenomena can be analyzed quantitatively.

Fig. 14 shows the model used for studying the effect of moderately conductive ground water interacting with a limestone and argillaceous sandstone interface. To simplify the analysis, the conductive water within each rock is assumed primarily to alter the loss tangent value without changing the velocity. Fig. 15 compares amplitude variation with four dipping angles for a fixed radar frequency (400 MHz) and four different antenna frequencies for a fixed dip angle. In the calculated synthetic radargrams, a rather distinctive reflection is produced from the contrast in the loss tangent even for the same

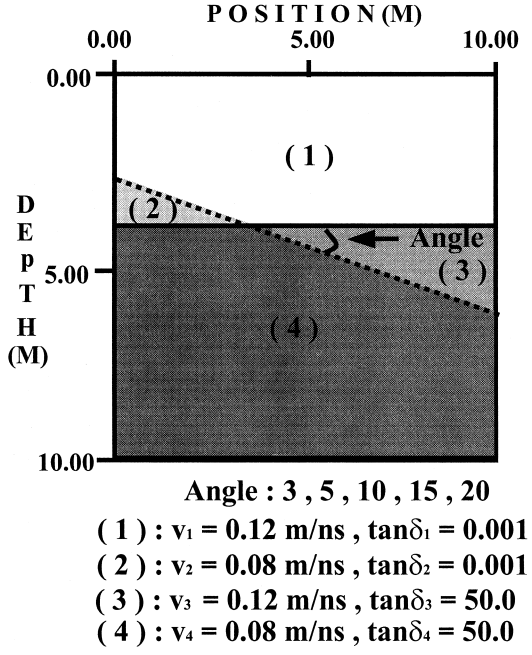

Fig. 14. Synthetic model used for amplitude and traveltime analysis. The solid line represents the water table. The dashed line represents the lithological boundary between limestone (upper layer) and argillaceous sandstone (lower layer). Common-shot radar data were collected along the surface. These four interfaces produce the corresponding reflections labeled in Figs. 15 and 16.

type of rock. The amplitude reduction caused by attenuation is rather distinguishable in Fig. 15b,d. For a fixed frequency, amplitude variation with incidence angle in Fig. 15a, and a shifting of amplitude decay due to the thin bed tuning effect in Fig. 15b are more apparent. For a frequency-dependent dielectric medium, the amplitude reduction is greater for a higher frequency (Fig. 15d) than for a lower frequency response. Frequency-dependent reflection coefficients can be identified in Fig. 15c. Fig. 15c and d exhibit the same behavior in amplitude variation with frequency across any type of interfaces.

Fig. 16 shows a comparison of travel time variations in reflection arrivals versus incidence angle at different dip angles among limestone/sandstone/water table interfaces and their variation at different frequencies. Rela-

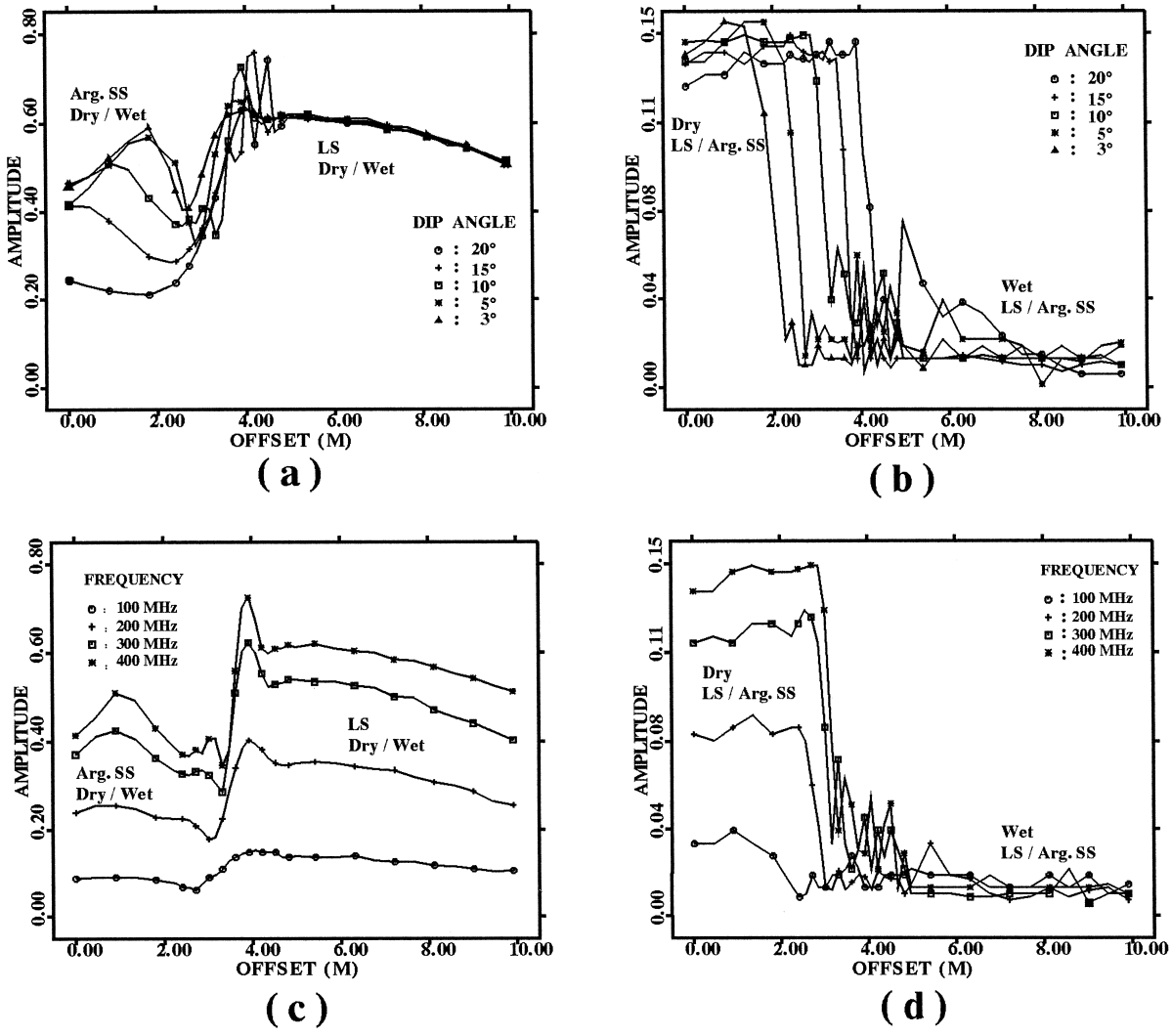

Fig. 15. The extracted amplitude responses as functions of offset for reflections produced from the model in Fig. 14. Amplitude variation studies for various dip angles for a dominant frequency of 400 MHz are shown in (a) and (b). The variations in amplitude vs. antenna frequencies are shown in (c) and (d). The dip angle of the boundary is fixed at 10°. The variations of reflected radar amplitudes associated with four different types of interfaces are labeled. These interfaces were produced mainly by the difference in water content over a limestone/sandstone interface or by the difference in attenuation when the water table is in the same rock unit.

tively small variation of arrival time occurs as the frequency is altered in the computed reflections (see Fig. 16c and d). The early arrival results from physical dispersion according to which phase velocity (therefore group velocity) is greater than the non-dispersive velocity for the entire range of frequencies. Such dispersion phenomena for argillaceous sandstone are more distinguishable than the responses from limestone when measuring against the reflected energies produced by the attenuating interface.

4.7. Field data application

To confirm the feasibility of our radar simulation scheme, we present a synthesis of GPR

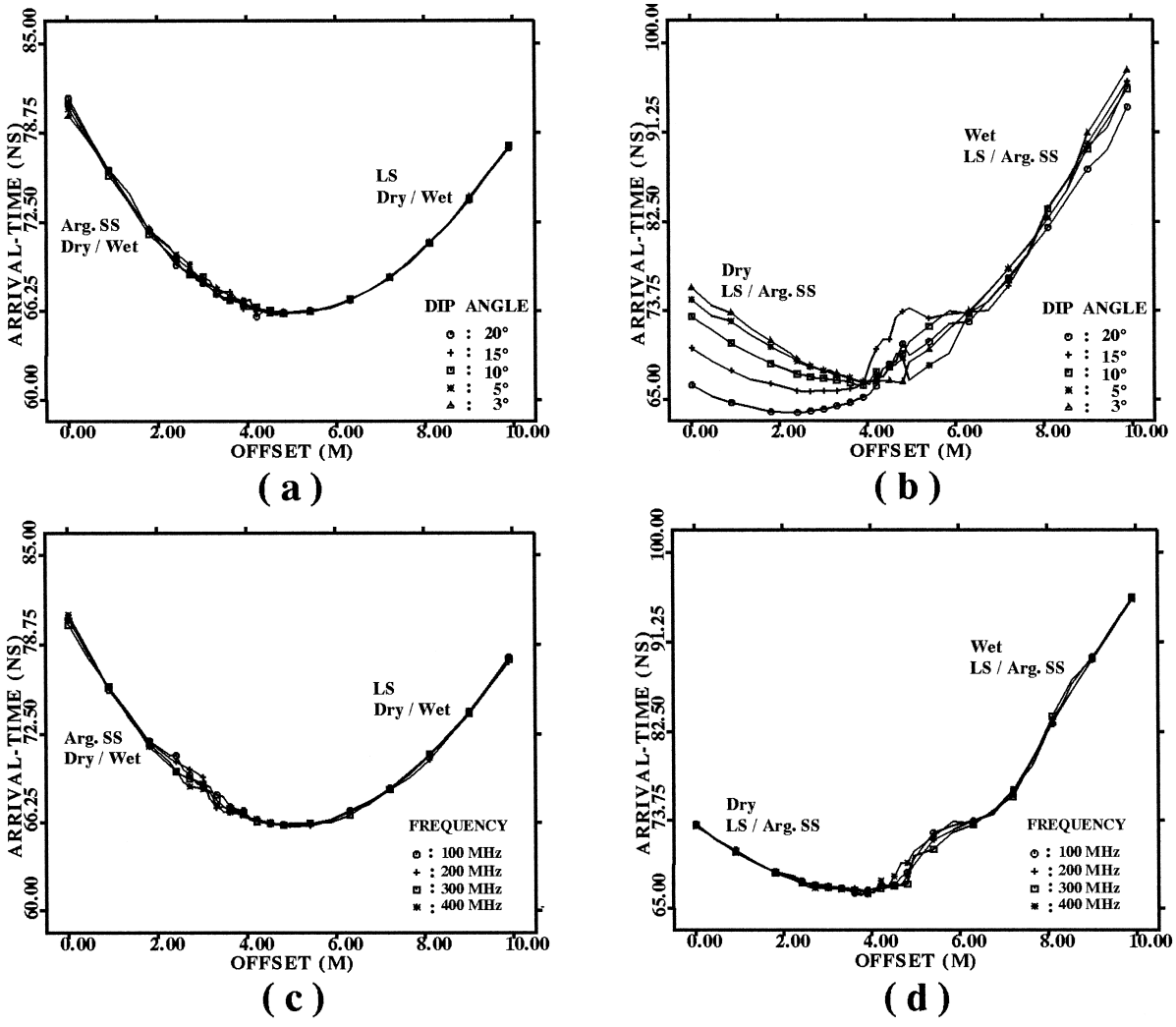

Fig. 16. Travel time responses as functions of offset for reflections produced from the model of Fig. 14. Travel time variation studies for various dip angles and antenna frequencies are shown in (a) to (d). The variations of reflection times for various situations are labeled. The dispersion phenomena is indicated by arrival time variations with frequency from different interfaces are shown in (c) and (d).

field data from data collected on a gymnasium construction site on the campus of NCCU. The geological environment is primarily un-consolidated Quaternary fluvial/aeolian sediments. Geological information obtained from geological investigations, drilling, and trenching indicate that the Shan-Hsiung and Mei-Shan formation are the two major layers covering the entire campus area. The excavation during construction of the basement reveals the uppermost (approximate 12 m) part of the stratigraphic units. The geological column consists of 1.0–1.5 m weathered lateritic soil overlying 2.0–7.0 m of poorly sorted gravel interbedded with sand and clay (Shan-Hsiung Fm.), and the water-bearing Mei-Shan Fm. primarily composed of yellowish sandy clay and blue to grayish silty clay. A wedge-shaped irregular thickness of siltstone is interfingered with a clay layer within the Mei-Shan Fm.

Fig. 17 presents one of the data sets acquired during the Fall of 1994. The GPR survey was conducted using the Sensors and Software pulseEKKO IV digital acquisition system. A 100 MHz, 400-V power antenna with a 3-m transmitter-to-receiver antenna separation was used; the trace separation was 20 cm; the time sampling increment was 0.8 ns; and 128 traces were stacked at each receiver location. Spectral analysis indicates a downshift in the dominant frequency to approximately 50 MHz even though 100 MHz antennas were used. Therefore, synthetic radargrams with dominant frequency of 50 MHz were generated to simulate the field data. Such downshift in frequency content of radar signal indicates a relative strong near-surface attenuation effect. The highly attenuative near-surface material with moderately varying stratigraphy features, including horizontally layered depositional units and locally lapping beds, can be observed from the excavation profiles. The data set has large lateral amplitude variations caused by the interference between arrivals from scattered radar waves, lateral face changes, and variation in attenuation. The relatively weak reflections around 100 ns are almost indistinguishable due to a smearing effect from background scattered energy. However, the reflected energies with spatially varying amplitude are revealed when the same data is displayed with polarity reversal as shown in Fig. 17b.

The potential of the current GPR modeling scheme is demonstrated when simulating and interpreting the field data. The underground structural features were first estimated with an

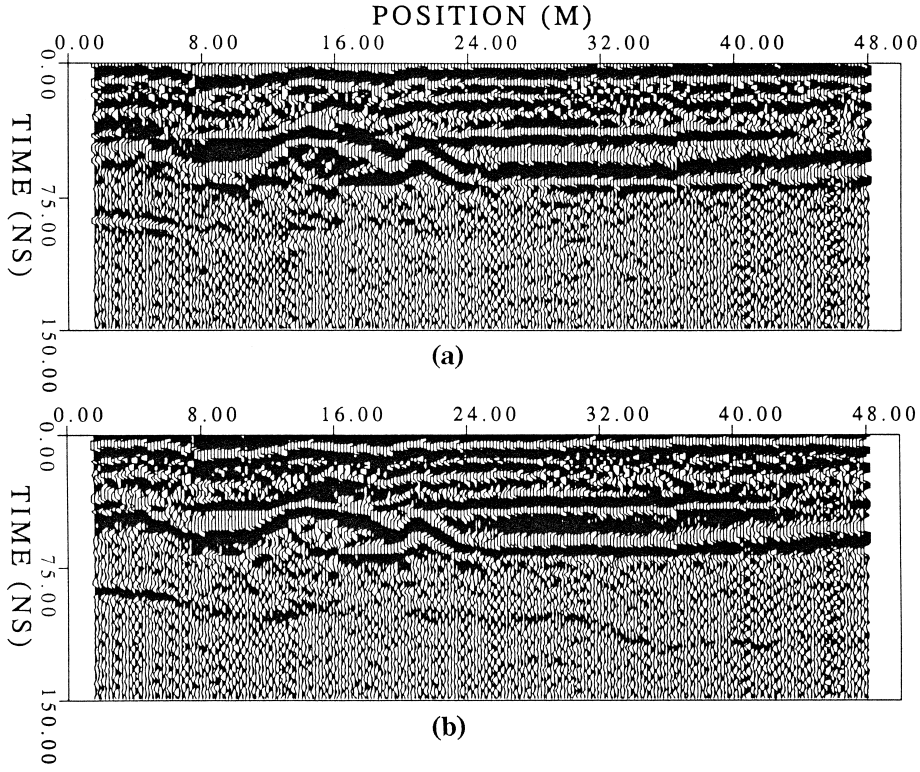

Fig. 17. Field data acquired at a construction site on the NCCU campus. The bistatic radar profile is acquired with an antenna separation of 3 m. The radar signals are highly attenuated such that there are no coherent reflections below 150 ns. (a) The radargrams are gained and clipped to display a weak reflection appearing around 100 ns. (b) The same data are displayed with the reversed polarity.

in-house developed FK migration scheme under a constant background velocity. During the iterative modeling process, FK modeling (Zeng et al., 1995) was occasionally used to check impedance contrast whenever there was large change in geometry and velocity. To save efforts in modeling and computational time, the synthetic data produced by the exploding-reflector concept was used first to fit both primary reflection time and amplitude observed in the NMO corrected field data. The final step is the modeling of actual bistatic radargrams with a constant-offset finite-difference modeling scheme to obtain a satisfactory result (Fig. 18).

Direct radar waves in the air are not part of the synthetic responses. The model parameters and reflector geometries were obtained by initially fitting the structural geometry based on reflection time and then iteratively altering the attenuation distribution based on reflection amplitudes. Although the current simulation scheme is capable of modeling backscattered radar energy from changing media properties, such scattering energy is not presently included. The final model (Fig. 19) predicts the main features, and even some small wave interference patterns are well simulated. The relatively small reflections generated from differences in attenuation and dielectric properties between two clay units within Mei-Shan Fm. is also adequately modeled. According to the modeling result, an extremely thin silt bed lies on top of a gravel formation between stations at 24 to 48 m at depth of 1.25 m. The silt layer produces a fairly large amplitude due to thin-bed (tuning) effects. Radar signal loss and amplitude fluctuations were significant even for small changes in thickness and conductivity during modeling. Si-

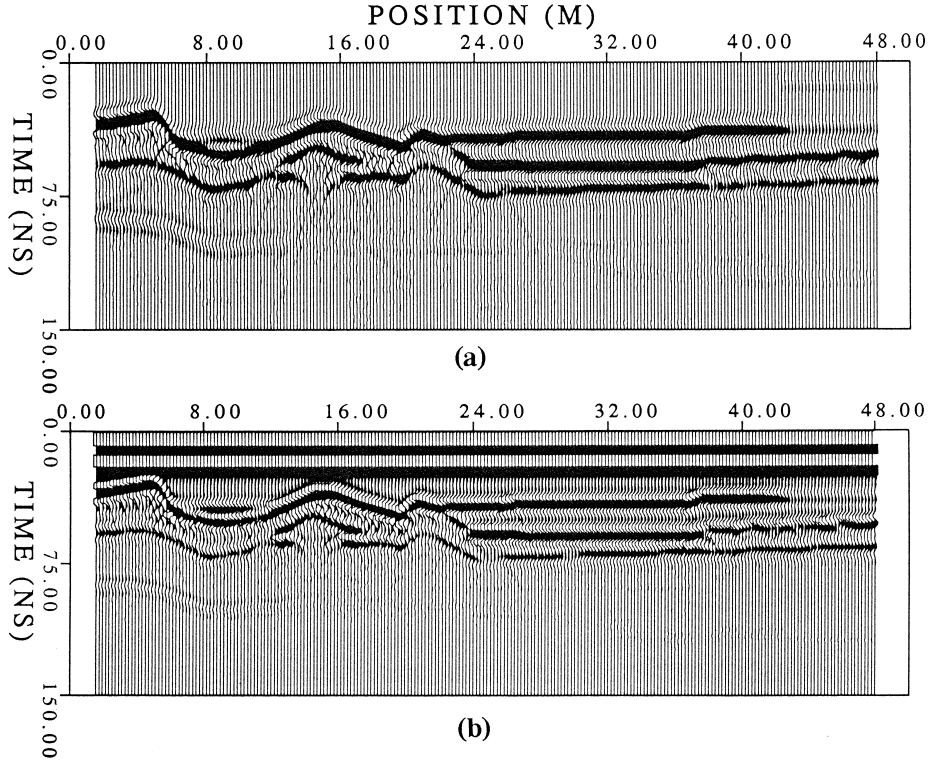

Fig. 18. Synthetic radar responses generated from two different simulation schemes. (a) Direct waves in the ground are not synthesized in the monostatic radargrams simulator based on the exploding-reflector concept. (b) A synthetic bistatic radar time section is generated from a generalized finite-difference scheme. Fig. 19 presents the final model.

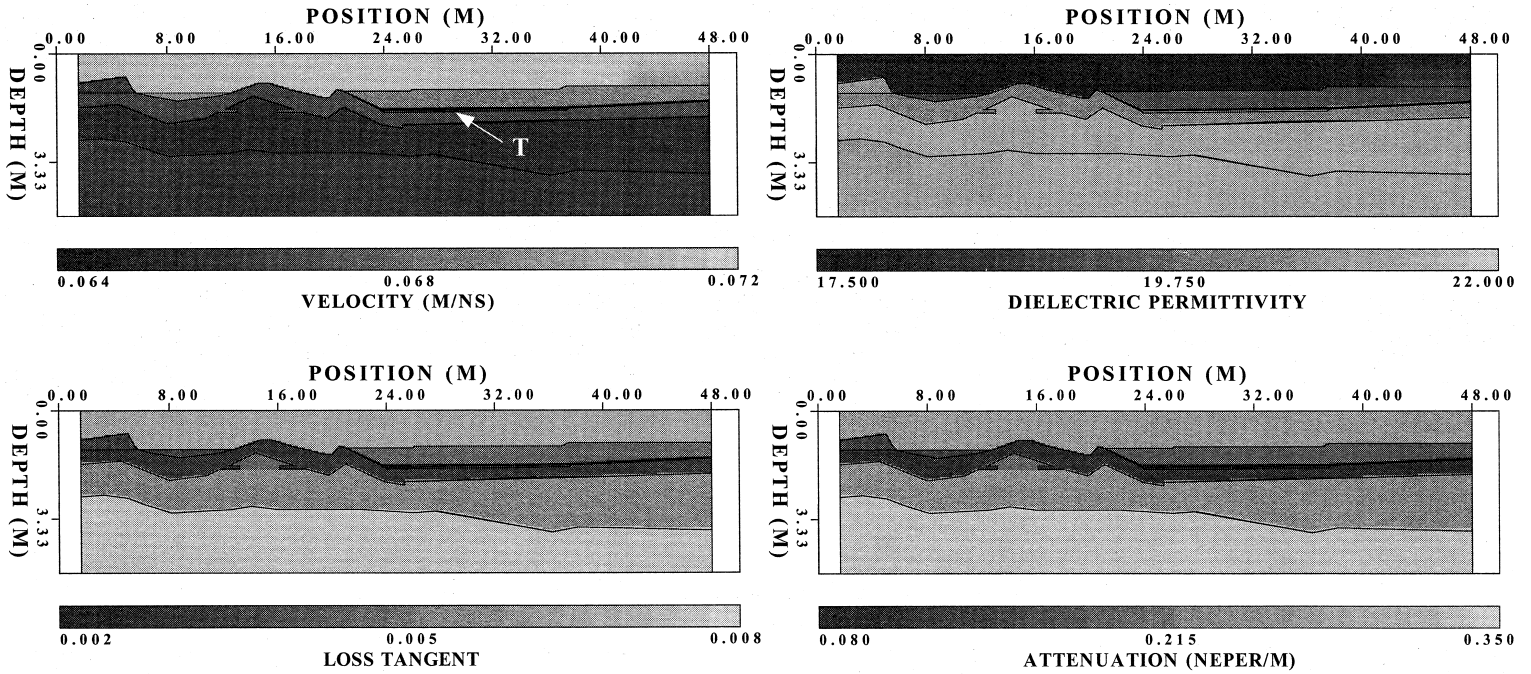

Fig. 19. The final model obtained form finite-difference modeling. Velocity (upper right), loss tangent (lower right), their corresponding relative dielectric permittivity (upper left) and attenuation (lower left) distributions used to produce the finite-difference modeling result. T denotes the thin bed.

multaneous correlations of field data from monostatic modeling via FK modeling and bistatic modeling through finite-difference simulation schemes provide better constraints on the final model. The model was also used to model other radar profiles collected in the same area with different offsets. The results correspond well to those of the model.

5. Discussion and conclusion

Numerical algorithms for modeling GPR data are developed, tested and implemented for 2-D media. We have implemented, applied and compared three algorithms for numerical synthesis of monostatic and bistatic GPR profiles. Implementing the attenuation mechanism provides a highly effective technique for simulating more realistic earth media. The numerical scheme naturally includes typical parameters to accurately describe the physical properties, e.g., velocity and attenuation, to mimic radar wave propagation through attenuative, near-surface ground materials. The approach presented herein may be an adequate tool for resolving geophysical problems and to interpret radargrams quantitatively. Attenuation effects considerably alter the recorded GPR wave fields.

The current implementation of composite absorbing mechanisms works quite well with the decoupled TE mode radar propagation problems. The method effectively suppresses both incoming and outgoing waves within a relatively narrow absorbing region. One distinct feature is that the width of the absorbing zone is inversely proportional to the dominant frequency used. Thus, the limitations of incidence angle and frequency-dependent properties can be alleviated in our approach. Optimal absorbing boundary conditions include floating, fixed one-way paraxial wave approximations, damping the radar wave field dynamically, or by adjusting attenuation properties of the model. The impedance contrast in the absorbing buffer region can also be used to minimize reflections. However, the algorithm requires some further investigation if coupled electromagnetic wave fields are considered.

We have demonstrated how to implement the simulation of GPR data by solving the damped scalar wave equation via staggered-grid finite-difference approximation. Accurately modeling of attenuation, large velocity contrast, and loss tangent variations of near-surface ground materials is also demonstrated through comparisons with field data. The wave-based modeling automatically includes full wave field phenomena (diffraction) for electric properties (velocity and attenuation) and geometrically complicated subsurface structures. Any other numerical means of solving the scalar lossy wave equation may also be used. Finite-element or pseudospectral solutions of Maxwell's equations can also handle arbitrary dielectric constants and attenuation variations. Implementing staggered-grid pseudospectral approximation (Chen, 1996) for dispersive and attenuative viscoacoustic material through memory variables is a highly promising alternative to account for the intrinsic attenuation.

Synthetic common-shot, constant-offset radar profiles based on actual transmitter-to-receiver configurations and based on the exploding-reflector concept were demonstrated to mimic different types of radar survey geometries. Computations in the second scheme are relatively fast except that air and ground waves are not included. Also, some caution should be exercised when modeling multiple radar reflections. The proposed numerical schemes can accurately model both monostatic and bistatic data, including reflection profiling, wide-angle reflection and refraction (WARR), and transillumination modes. Analyzing amplitude and arrival time variation with an offset provides a quantitative estimation of electric properties, attenuation, and dispersion behavior, possibly leading to an indirect measure of porosity, fluid content, and permeability of near-surface ground materials.

The discrepancies arising between the field observations and synthetic profiles may be attributed to two main causes. The first is the fact that the transmitter and receiver directivity patterns are not explicitly considered in the current scheme. However, an equivalent solution can be obtained if the antenna radiation pattern is known. The superposition of a few single electric sources may yield satisfactory results based on the direct numerical grid method, which is similar to the simulation of various seismic sources (Chen and McMechan, 1992a,b; Chen, 1996). The second is the fact that most scattering arrivals produced from gravel and other randomly scattered buried objects are not considered. This will be one of the subjects in our future research. Corrections accounting for computed 2-D geometrical spreading and attenuation to 3-D cases are not included; however, those are expected to be less important.

The GPR simulator developed herein is a useful and a highly effective tool for future developments in GPR data modeling and processing projects. The capability of extracting electrical properties from field data have a certain potential for lithological identification and discrimination. Modeling of coupled electromagnetic vector wave field responses is feasible and is the next necessary step. The same wave field extrapolation scheme can be also used for wave field migration in imaging near-surface structures for engineering and environmental applications. Three-dimensional forward simulation of GPR is also necessary to account for 3-D propagation effects which are commonly observed in the radar section.

Acknowledgements

The research leading to this paper was supported by the National Science Council of the Republic of China (ROC) under grant number NSC 84-2621-P-194-003B. The field data were collected using a pulseEKKO IV system manufactured by Sensor and Software. The computing resource for this research was performed at Sparc workstations at the Institute of Seismology and Applied Geophysics (IOS/IAG). The authors are grateful to Jame B. Cole, editor-in-Chief T. E. Owen and an anonymous reviewer for their constructive comments and suggestions on the manuscript.

References

Adhidjaja, J.I., Hohmann, G.W., Oristaglio, M.L., 1985. Two-dimensional transient electromagnetic responses. Geophysics 50, 2849–2861.

Alford, R.M., Kelly, K.R., Boore, D.M., 1974. Accuracy of finite difference modeling of the acoustic wave equation. Geophysics 39, 834–842.

Annan, A.P., 1973. Radio interferometry depth sounding: Part I. Theoretical discussion. Geophysics 38, 557–580.

Bevan, B., 1991. The search for grave. Geophysics 56, 1310–1319.

Brekhovskikh, L.M., 1960. Waves in layered media, Academic Press, New York, 561 pp.

Bogorodsky, V.V., Bentley, C.R., Gudmandsen, P.E., 1985. Radioglaciology. D. Reidel Publishing Co.

Cai, J., McMechan, G.A., 1995. Ray-based synthesis of bistatic ground-penetrating radar profiles. Geophysics 60, 87–96.

Cerjan, C.D., Kosloff, D., Kosloff, R., Reself, M., 1985. A non-reflecting boundary condition for discrete acoustic and elastic wave equations. Geophysics 50, 705–708.

Chen, H.W., McMechan, G.A., 1992a. Computation of multi-attribute seismic wave fields by solution of the elastodynamic equations. Bull. Seismol. Soc. Am. 82, 1134–1143.

Chen, H.W., McMechan, G.A., 1992b. Effects of source configuration on seismograms. J. Seismol. Expl. 1, 207–215.

Chen, H.W., 1996. Staggered-grid pseudospectral viscoacoustic wave field simulation in 2-D media. J. Acoustic Soc. Am. 67, 1529–1540.

Claerbout, J.F., 1985. Imaging the Earth's Interior. Blackwell, Pala Alto, CA, 398 pp.

Clayton, R., Engquist, B., 1977. Absorbing boundary conditions for acoustic and elastic wave equations. Bull. Seismol. Soc. Am. 67, 1529–1540.

Coggon, J.H., 1971. Electromagnetic and electrical modeling by the finite-element method. Geophysics 36, 132–155.

Dablain, M.A., 1986. The application of higher-order dif-

ferencing to the scalar wave equation. Geophysics 51, 54–66.

Davis, J.L., Annan, A.P., 1989. Ground-penetrating radar for high-resolution mapping of soil and rock stratigraphy. Geophys. Prosp. 37, 531–551.

Hohmann, G.W., 1975. Three-dimensional induced polarization and electromagnetic modeling. Geophysics 40, 309–324.

Goldman, M.M., Stoyer, C.H., 1983. Finite-difference calculations of the transient field of an axially symmetric earth for vertical magnetic dipole excitation. Geophysics 7, 953–963.

Goldman, D., 1994. Ground-penetrating radar simulation in engineering and archaeology. Geophysics 59, 224–232.

Israeli, M., Orszag, S.A., 1981. Approximation of radiation boundary conditions. J. Comp. Phys. 41, 115–135.

Kosloff, R., Kosloff, D., 1986. Absorbing boundaries for wave propagation problems. J. Comp. Phys. 63, 363–376.

Kreiss, H.O., Oliger, J., 1972. Comparison of accurate methods for the integration of hyperbolic equations. Tellus 24, 199–255.

Kuo, J.T., Cho, V.-H., 1980. Transient time-domain electromagnetics. Geophysics 45, 271–291.

Levander, A.R., 1988. Fourth-order finite-difference P-SV seismograms. Geophysics 53, 1425–1436.

Livelybrooks, D., Fullager, P.K., 1994. FDTD2D+ A finite-difference, time-domain radar modeling program for two dimensional structures. 5th Internat. Conf. Ground Penetrating Radar, Expanded Abstracts, Univ. of Waterloo, 87–100.

Mitchell, A.R., 1969. Computational methods in partial differential equations. Wiley, New York, 255 pp.

Nabighian, M.N., 1991. Electromagnetic methods in applied geophysics-Theory, Vol. 1, SEG publication. Tulsa, OK, 513 pp.

Oristaglio, M.L., Hohmann, G.W., 1984. Diffusion of electromagnetic fields in a two-dimensional earth: a finite-difference approach. Geophysics 49, 870–894.

Pridmore, D.F., Hohmann, G.W., Ward, S.H., Sill, W.R., 1981. An investigation of finite-element modeling for electrical and electromagnetic data in three dimensions. Geophysics 46, 1009–1024.

Raiche, A.P., 1974. An integral equation approach to 3D modeling. Geophys. J. R. Astr. Soc. 36, 363–376.

Roberts, R.L., Daniels, J.J., 1994. Finite-difference time domain (FDTD) forward modeling of GPR data. 5th Int. Conf. Ground Penetrating Radar, Expanded Abstracts. Univ. of Waterloo, 185–204.

Robertsson, J.O.A., Blanch, J.O., Symes, W.W., 1994. Viscoelastic finite-difference modeling. Geophysics 59, 1444–1456.

Sochachi, J., Kubichek, R., George, J., Fletchchen, W.R., Smithson, S., 1987. Absorbing boundary conditions and surface waves. Geophysics 52, 60–71.

Silvester, P., Haslam, C.R.S., 1972. Magnetotelluric modeling by the finite-element method. Geophys. Prosp. 20, 872–891.

Stolt, R.H., 1978. Migration by Fourier transform. Geophysics 43, 23–48.

Stratton, J.A., 1941. Electromagnetic theory. McGraw-Hill, New York, 615 pp.

Szaraniec, E., 1976. Fundamental functions for horizontally stratified earth. Geophys. Prosp. 24, 528–548.

Szaraniec, E., 1979. Towards unification of geophysical problems for horizontally stratified media. Geophys. Prospect. 27, 576–583.

Telford, W.M., Geldart, L.D., Sheriff, R.E., Keys, D.A., 1976. Applied Geophysics, Cambridge Univ. Press, London, 860 pp.

Topp, G.C., Davis, J. L, Annan, A.P., 1980. Electromagnetic determination of soil water content: measurements in coaxial transmission lines. Water Resources Res. 16, 574–582.

Ursin, B., 1983. Review of elastic and electromagnetic wave propagation in horizontally layered media. Geophysics 48, 1063–1081.

von Hippel, A.R., 1954. Dielectric and Waves. Chapman & Hall, Wiley, New York, 284 pp. (Companion book: Dielectric materials and applications, pp. 276–277).

Wannamaker, P.E., Hohmann, G.W., San Filipo, W.A., 1984. Electromagnetic modeling of three-dimensional bodies in layered earth using integral equations. Geophysics 49, 60–74.

Wang, T., Tripp, A.C., 1996. FDTD simulation of EM wave propagation in 3-D media. Geophysics 61, 110–120.

Weidelt, P., 1975. Electromagnetic induction in three-dimensional structures. J. Geophys. 41, 109–885.

Wright, D.L., Bradley, J.A., Hodge, S.M., 1989. Use of a new high-speed digital data acquisition system in airborne ice sounding. IEEE Trans. Geos. Rem. Sens. 27, 561–567.

Yee, K.S., 1966. Numerical solution of initial boundary value problems involving Maxwell's equations in isotropic media. IEEE Trans. Antennas Propagat. AP 14, 302–307.

Zeng, X., McMechan, G.A., Cai, J., Chen, H.W., 1995. Comparison of ray and Fourier methods for modeling monostatic ground-penetrating radar profiles. Geophysics 60, 1727–1734.